Romero-Resendiz, L.; Rossi, M.; Álvarez, A.; García-García, A.; Milián, L.; Tormo-Mas, M.; Amigó, V. (2022). Microstructural, mechanical, electrochemical, and biological studies of an electron beam melted Ti-6Al-4V alloy. Materials Today Communications. 31:1-14. https://doi.org/10.1016/j.mtcomm.2022.103337

Microstructural, mechanical, electrochemical, and biological studies of an electron beam melted Ti-6Al-4V alloy

L. Romero-Resendiz[a,1,*], M.C. Rossi[b,1], A. Álvarez[b], A. García-García[b], L. Milián[c], M.Á. Tormo-Más[d], V. Amigó-Borrás[b]

[a] Instituto de Investigaciones en Materiales, Universidad Nacional Autónoma de México, Circuito exterior S/N, Cd. Universitaria, A. P. 70-360, Coyoacán, C.P. 04510, Mexico.
[b] Universitat Politècnica de València, Instituto de Tecnología de Materiales, Camino de Vera s/n, 46022 Valencia, Spain.
[c] Departamento de Patología, Facultad de Medicina y Odontología, Universitat de València, Valencia, Spain
[d] Hospital de Infección Grave, Hospital Universitari i Politècnic La Fe, Instituto de Investigación Sanitaria La Fe, Avenida Fernando Abril Martorell, Valencia, 46026, Spain
[1] Contributed equally to this work.
* Corresponding author. E-mail address: liliana.rom7@comunidad.unam.mx

Abstract

This work studied the feasibility of an electron beam melting (EBM) Ti-6Al-4V alloy as a biomaterial for implants. Comparisons were made with a wrought forged Ti-6Al-4V alloy. The objective of this work was a detailed description of the microstructural and surface roughness effects on mechanical, electrochemical, and in-vivo biological performances. The EBMed condition showed higher mechanical properties, as well as higher electrochemical and ion release rates. These results were mainly influenced by the lamellar grain morphology and complex crystallographic texture of the EBMed alloy compared to the forged one. The higher area average roughness of the EBMed condition boosted the adhesion, proliferation, and biofilm formation of osteosarcoma (MG63), Staphylococcus epidermidis (S. epidermidis), and Staphylococcus aureus (S. aureus). The mechanical, ion release, corrosion, and in-vivo biological results in both studied conditions met the requirements for orthopedic and dental biomaterials. Thus, both studied conditions of the Ti-6Al-4V alloy are feasible candidates for biomedical implants. However, the forged

condition is more recommended for patients with clinic stories related to S. epidermidis and S. aureus illnesses.

Keywords
Ti-6Al-4V, texture, ion release, corrosion, cytotoxicity, cell proliferation

1. Introduction

The aging of the population is a worldwide known phenomenon that increases the number of total hard tissue replacements or necessary fixations, such as the hip and knee. Metals are still the load-bearing material of choice for structural prostheses because of their excellent mechanical properties and cost [1]. The advantages of biomedical Ti alloys have been widely reported due to their higher biocompatibility and suitable mechanical properties compared to other metallic materials [2]. From Ti alloys, Ti-6Al-4V alloy is one of the most popular in the biomedical field due to its combination of acceptable mechanical properties, corrosion resistance, and biocompatibility [3,4]. The higher corrosion resistance of Ti-6Al-4V alloy, in comparison with Co-Cr and SUS316L, was reported [5]. Besides, pitting corrosion due to the breakdown of the passivation layer generally does not occur in this alloy in the presence of amino acids or proteins in Hanks or Ringer's solution media [6–9], or like implants on the back muscle of rabbits [7]. Additionally, the passivation behavior of Ti-6Al-4V has been reported similar to Ti-6Al-4Nb, Ti-6Al-4Fe, and Ti-5Al-2.5Fe [10]. Furthermore, it was found that the balance between α and β phases in Ti-6Al-4V alloy allows good mechanical properties achievement [11].

Regarding the Ti–6Al–4V production, it is found that the traditional routes to obtain casting and wrought alloys, show several limitations. Heterogeneities as segregation are commonly found in cast Ti ingots [11,12] and long-time homogenization heat treatments might be necessary. However, the Ti reactive nature at elevated temperature does not allow the application of those treatments in a cost-benefit way [11]. Another drawback of casting is the contamination of ingots with high-density inclusions (HDI) and high interstitial defects (HID), which alter the mechanical properties of Ti alloys [11,13,14]. On the other hand, the conventional wrought Ti alloys imply several melting cycles to overcome the purity shortcomings of the cast materials [15]. The re-melting cycles are followed by

thermo-mechanical routes as forge or milling and heat treatments, which increase the mechanical properties compared to casting components but also their time production [15]. As a solution to the aforementioned problems, additive manufacturing (AM) has shown advantageous microstructural control by modifying the processing parameters [16]. Furthermore, AM allows large or small dimensional near-net-shapes production [17], which is a valuable attribute for producing devices of demanding geometry and size without requiring consecutive thermo-mechanical processes. Due to the above, AM is one of the most promising fabrication techniques to produce Ti-components [16,17]. Moreover, powder metallurgy by AM techniques is widely used for dental and orthopedic devices because porous microstructures trigger the anchorage of the implant to the organic tissue of bone [18–21].

Electron beam melting (EBM) is an AM technique that selectively melts the metal powder using an electron beam to form layers of the final component [22]. Among the benefits of EBM are the rapid production, cost-effectivity, accurate geometrical control, adequate organic tissue-implant interfaces, and low content of interstitial elements on the Ti-6Al-4V alloy [4,16,23]. EBM has been used to manufacture many Ti alloys for biomedical purposes. Most of these investigations have been focused on developing a comprehensive understanding of the processing-microstructure-properties relationships on Ti-6Al-4V [22,24–27]. Regarding the mechanical performance, the lamellar grain morphologies and their finer thickness are related to higher strengthening [22,25]. The Ti-6Al-4V produced by EBM has also been compared with its cast counterpart, finding at least two orders greater dislocation density in the EBMed alloy [27]. This resulted in higher hardness through EBM compared to the conventional route. Concerning corrosion performance, the EBMed Ti-6Al-4V immersed in phosphate-buffered saline solution slightly improved its corrosion resistance compared to the wrought condition [28]. This was related to a homogeneous distribution of alloying elements that resulted in decreased galvanic effect between phases in the EBMed alloy. Compared to the wrought and selective laser melting (SLM) conditions, the best performance of the EBMed alloy under crevice corrosion and electrochemical corrosion at electrode potential higher than 1.5 V was also reported [29]. Besides, Ti-6Al-4V Alloy with fine lamellar grain morphologies reported superior corrosion resistance than coarse and acicular morphologies immersed in 3.5 wt.%

NaCl [30]. The abovementioned reports studied the mechanical and corrosion properties of the EBMed Ti-6Al-4V but scarce information has been reported related to its biocompatibility on alive cells.

One of the main aspects that leads to the good acceptance of one metallic biomaterial is the biological interaction [31–33]. For the bone-implant interface to integrate properly (osteointegration), there is a need for bone cells to be differentiated, adhered to, and proliferate on the surface of implant materials [34]. Such biological integration quality is influenced by the microstructure and morphology of the implant [35,36]. Accordingly, the microstructural features and biocompatibility of the EBMed Ti-6Al-4V must be investigated before clinical applications.

Another factor to consider in metallic implants is the likelihood of periprosthetic infection (PPI). The PPI, is the colonization and growth of microorganisms in the implant, causing a symptomatological picture in the patient. The PPI could trigger prosthesis failure. A replacement larger than the original prosthesis might be necessary due to the loss of infected tissue and the performing of resection of healthy tissue to ensure that superinfection does not develop [37]. The PPI forms part of the microbiota of the skin and is known in medical microbiology as opportunistic pathogens, from where the Staphylococcus epidermidis (S. epidermidis) and the Staphylococcus aureus (S. aureus) cause two-thirds of the infections. About 2% of the incidence of this infection results in total arthroplasty of the knee [37]. The cost derived from each treatment per patient varies between 59,601-65,439 United States Dollars (USD) (10 times more than its basal price) [38]. Therefore, the estimated economic impact of the revision surgery for infections in the US was 1,620 million USD [37]. Due to the above, it is fundamental to investigate the performance of the Ti-6Al-4V alloy in contact with S. epidermidis and S. aureus. It has been demonstrated that EBMed Ti-6Al-4V alloy supports cell attachment, growth, and differentiation [39,40], but it has not been tested on S. epidermidis and S. aureus cultures.

Based on the above, this paper aims to evaluate the mechanical, corrosion, and biological assessments of the Ti-6Al-4V alloy manufactured by EBM and compare it with a forged reference condition. The results are explained in terms of the microstructural features of the alloy. No previous literature was found studying the performance of S. epidermidis (RP62A), S. aureus (V329), and osteosarcoma cells on EBMed Ti-6Al-4V

alloy. These results will improve the knowledge of Ti-6Al-4V tested on different in-vivo biological environments. The correlation of microstructural features with the mechanical, corrosion, and biological behaviors will also serve as a basis for the design of other biomedical alloys.

2. Experimental procedure

2.1. Microstructural evaluation

Commercially available forged (reference material) and EBMed Ti-6Al-4V ELI alloys were obtained from Zimmer Biomet and AIDIMME companies, respectively. From section 1, the conventional wrought forged Ti alloys are mechanically and purity advantageous over their conventional casting counterparts. The reference forged Ti alloy was selected to guide on the feasibility as biomaterial of the relatively new EBM process and the most advantageous conventional production route. The geometry of raw plates was 60 mm diameter, 5 mm thick; and 30 mm of diameter and 10 mm thick, for forged and EBMed materials, respectively. Before the microstructural examination, samples were embedded in conductive resin and subjected to a conventional metallographic preparation. Mirror finishing appearance was obtained with colloidal silica suspension of 0.05 μm in particle size. An ultrasonic bath with acetone was used for 20 min to clean the samples. Kroll´s reagent was used to reveal the grains. The morphological and microstructural observations were done by using optical and scanning electron microscopes (Nikon Eclipse LV100 and Zeiss Ultra55 FESEM, respectively). For Electron Backscattering Diffraction (EBSD), the material was prepared using conventional metallographic preparation, followed by vibratory polishing with a VibroMet 2 machine, using a colloidal silica solution with a particle size of 0.3 μm. Ultrasonic cleaning was used for removing surface impurities. The EBSD analysis was carried out in a Zeiss Auriga model scanning electron microscope with an HKLNordlys EBSD detector (15 KV). To study surface morphology and surface roughness of the forged and EBMed Ti-6Al-4V alloys, a Filmetric Profilm3D profilometer was used over a large scanning area (850 x 800 μm). The parameters to evaluate the surface roughness: arithmetic average roughness (S_a), root mean square roughness (S_q), skewness (S_{skw}), and kurtosis (S_{kur}) were calculated based on UNE ISO, 25178-2:2013. The percentage of present phases was obtained by a Rietveld refinement of

X-Ray Diffraction (XRD) peaks by using Material Analysis Using Diffraction (MAUD) software by Radiographema 2.99 version. These results were obtained by using a Bruker X-ray diffractometer D2 Phaser with a Cu-Kα source radiation, 30 KV and 10 mA as the voltage and current conditions, respectively. The measurements were collected in a 2θ range from 20° to 90° with a step size of 0.02° each 10 s.

2.2.Mechanical characterization

To evaluate the elastic modulus (E) of the forged and EBMed Ti-6Al-4V alloys, the non-destructive impulse excitation technique (IET) was carried out by the Sonelastic equipment. The software ATCP Sonelastic 3.0 was used to analyze the data. At least 3 elastic modulus measurements were obtained per condition studied. To remove stress concentrators before tensile tests, the surface of all the samples was previously subjected to computer numerical control (CNC) milling. The geometry of the samples was 2 x 1 x 10 mm on width, thickness, and length, respectively. Tensile tests were realized on a Shimadzu Autograph AG-100 KN Xplus universal testing machine at a constant strain deformation of 1 mm/min. At least 3 measurements were obtained per studied condition. Ultimate (UTS) and yield (YS) strengths were obtained from the tensile test plots. The YS was determined using the well-known 0.2% strain offset criterion. The software Trapezium X was used for plotting tensile measurements. A Centaur durometer model HD9-45 was used for microhardness measurements ($HVN_{0.3}$). Samples with 5 mm thickness were tested by applying 3 N for 15 s with the previous surface metallographic preparation. The hardness measurements were performed from the transversal plane on the forged samples, and in a random direction for the EBMed condition. At least 5 measurements were obtained per sample.

2.3. Ion release measurement

Before the ion release evaluation, samples were subjected to conventional metallographic preparation up to a mirror-like appearance. For the ion release study, three samples of each condition were immersed in 50 mL of Fusayama solution (pH of 5.27±0.11) and incubated for 730 h at 37ºC. The chemical composition of the artificial

saliva was 0.4 g/L of NaCl; 0.4 g/L of KCl; 0.8 g/L of $CaCl_2$; 0.7 g/L of NaH_2PO_4; 2.5 g/L of NaF; 0.005 g/L of Na_2S; and 1 g/L of urea. The testing conditions, i.e., fluoridated artificial saliva at 37ºC for 730 h, were selected to simulate the damage due to three daily 2-minute tooth brushings for 20 years in the oral environment. After incubation, the morphology of samples was studied under optical and scanning electron microscopes. Inductively coupled plasma optical emission spectrometry (ICP-OES) was performed using Varian-715ES equipment to measure the concentrations of Ti, Al, and V ions dissolved in the incubated medium.

2.4.Corrosion behavior

The evaluation of corrosion resistance was carried out for three samples of each alloy by a Metrohm Autolab PGSTAT204 potentiostat. Samples were subjected to standard metallographic procedures and cleaned using acetone before immersion. All the electrochemical tests were performed in 1M NaCl solution (pH of 7.0±0.3) using a three-electrode system; a saturated Ag/AgCl electrode (SCE) as the reference electrode, a platinum tip as the auxiliary electrode, and the samples of Ti-6Al-4V as working electrode. The Nova 2.1.2 software recorded the frequency response. Kinetic corrosion parameters were determined using the Tafel extrapolation method.

2.5.Biological assessment

Prior to the biological evaluation, the samples were cleaned in an ultrasound bath with acetone, ethyl alcohol, and deionized water for 60 min. Posteriorly, the samples were dried and sterilized at 121ºC for 20 min in an STE-8-D autoclave, Icanclave.

2.5.1. Cell culture

The human osteosarcoma cell line MG63 was used to investigate its biological effects on the Ti-6Al-4V alloy. The cells were cultured in 25 cm^2 flasks using minimum essential medium (MEM) supplemented with 1% pyruvate, 1% non-essential amino acids, 1% penicillin-streptomycin, 1% L-glutamine, and 10% of Fetal bovine serum (FBS). The flasks were held at 37ºC in a humidified atmosphere of 5% CO_2 until the culture reached

80-90% confluence. The number of cells and their viability before the biological tests were evaluated by the 0.4% trypan blue dye exclusion method using the EVE Automatic Cell Counter. A total of million live cells were obtained per milliliter with cell viability greater than 95%. For the culture media conditioning, Ti-6Al-4V samples were used for 7 days. At 24 hours, 500 µL aliquots were extracted and after 7 days, the rest of the medium (3 mL) was extracted. The aliquots obtained from the conditioned medium were used for the MTS toxicity test. This test was important to assess whether the conditioned culture medium could release toxic particles that affect cell viability.

2.5.2. MTS toxicity test

Toxicity tests were carried out on 10 forged and 10 EBMed disks of Ti-6Al-4V, as well as their respective positive controls, negative controls, and the blank without cells. A total of 65 wells for forged disks and 65 for EBMed disks were used. For each well, $7x10^3$ cells were seeded with 100 µL of culture medium. After 24 hours, this medium was removed and another 100 µL of the conditioned medium by the samples. A medium conditioned with latex as positive toxicity control, as well as MEM medium for the wells for blank and the negative control, were added. In all cases, the medium was supplemented with 10% SFB.

The MTS assay was performed by adding the CellTiter 96 AQ One Solution reagent containing a tetrazolium compound [3-(4,5-dimethylthiazol-2-yl)-5-(3-carboxymethoxyphenyl)-2-(4-sulfophenyl)-2H-tetrazolium, inner salt; MTS] and, an electron coupling reagent (phenazine ethosulfate, PES) to each well to determine the number of viable cells in the assay. Metabolically active cell dehydrogenase enzymes reduce this reagent producing a soluble formazan derivative in the culture medium that absorbs at 490 nm. The absorbance was measured with a plate reader, the absorbance value is directly proportional to the number of viable cells.

2.5.3. Cell adhesion and proliferation assay

Five samples with cells were seeded for 5 hours, and 72 hours for the cell adhesion and proliferation assays, respectively. The samples were incubated at 37ºC in a humidified atmosphere of 5% CO_2. In both cases, 12 well-plates and 1500 cells/cm^2 for each well were

used. Cells seeded on slides (Milicell EZ) were used as adhesion and proliferation controls. The cells were fixed using 2.5% glutaraldehyde. For the cell growth on the disks, a phosphate-buffered saline (PBS) solution with 0.02% eosin was prepared to study the cytoplasm. For the observation of the cell nucleus. 300 nM of 6-diamino-2-phenylindole (DAPI) were used. The samples seeded with cells and their respective controls were studied using the Leica DFC340 FX microscope. The number of cells was evaluated from images obtained by a Leica DFC420 microscope using the Image-Pro Plus tool. The data analysis was carried out using the GraphPad Prism software. An average of 10 images obtained from every set of three repeated samples for each Ti-6Al-4V condition or control material was considered for the statistical quantification of cells. The normalized ratio of proliferating cells in each sample was calculated relative to their respective control. The proliferation was quantified based on the blue-stained cells by the DAPI dye.

2.5.4. Bacterial strains and growth conditions

The bacterial strains used in this study were S. aureus V329 and S. epidermidis RP62A (ATCC35984), which are two strong biofilm-forming strains. Stocks were stored in Tryptone Soy Broth (TSB) from Scharlau containing 20% glycerol at -80 ºC. Before analysis, each isolate was subcultured twice on TSA plates to ensure viability. The inoculum was prepared by suspending 1 to 3 colonies in PBS (pH=7.3) from a 24 h culture. Cell density was adjusted to 0.5 McFarland standard providing 1.5 x 10^8 CFU/mL. The final calculation of CFU/mL was executed after the serial dilutions.

2.5.5. Biofilm formation by S. epidermidis and S. aureus on different surfaces

To test biofilm formation 24 well-plates (Sarstedt) were used and equipped with sterile different Ti-6Al-4V samples. The plates were filled with 1 mL of TSB supplemented with 0.25% glucose (Scharlau), which was inoculated with 20 µL of the inoculum suspension and with 3x10^6 CFU/mL. The biofilm grew 48 hours at 37ºC. After washing and introducing the well-plates in a new culture medium, sonication and vortical agitation were applied. Posteriorly, serial dilutions were grown in plates for 24 hours to finally calculate the number of CFU/cm^2.

2.5.6. Field Emission Scanning Electron Microscopy to investigate the bacteria adhesion and morphology.

The samples were inoculated with both colonies and incubated for 48h at 37ºC. The medium was then removed, and the samples were washed with PBS twice to discard unattached bacteria. To ensure the correct cryogenization of the samples, liquid nitrogen was introduced into the vacuum chamber. The sample was sublimated for 7 min at -90 °C and then coated with Pt by sputtering to ensure electronic conduction. Finally, images were taken in an FE-SEM ULTRA 55 from Zeiss equipped with sample preparation equipment for cryo-SEM PP3010T from Quorum technologies.

2.5.7. Statistical Analysis.

Quantitative biological experimental data such as cell viability and quantification, are reported as the mean ± standard deviation (SD). The SD was also used as an error bar in the figures and tables. For the multiple comparisons, one-way Analysis of variance (ANOVA) and Kruskal Wallis tests were used, depending on whether the groups compared presented a Gaussian distribution. Differences were considered statistically significant when the P-value was <0.05. Plot curves and bar graphs were generated using GraphPad Prism v.7, OriginPro 8.5, and Excel 16.0.14228.20216 software.

3. Results and discussion

3.1.Microstructural evaluation

Figure 1 shows microstructural studies carried out on the forged (reference material) and EBMed (work material) conditions of the Ti-6Al-4V alloy by XRD, OM, SEM, and EDS. In Fig. 1a, the main peaks related to the α-Ti and β-Ti phases were identified. It is well-known that the Ti-6Al-4V alloy is biphasic due to the presence of Vanadium as an isomorphous β-stabilizer [41,42]. Compared to the forged condition, an increment in intensity can be seen at the peak at 40.4° of the EBMed condition, which corresponds to the (101) plane of α-Ti. This suggests a higher density of α-Ti crystals with preferred orientation to the (101) plane. This is an expected phenomenon on Ti-6Al-4V when

obtained by EBM [24]. On the other hand, the higher intensity of the α-Ti peaks suggests a greater content of this phase in the microstructure compared to the β-Ti.

Figure 1b,e obtained by OM depicts the morphology of the α-Ti and β-Ti phases in both studied conditions. In the forged condition (Fig. 1b) the strain path can be observed by elongated grains parallel to the forged direction (FD). In Fig. 1b is also visible a higher presence of α-Ti phase (light phase) in comparison with the β-Ti (dark phase), which was indicated by the bigger XRD peaks intensity of α-Ti (Fig. 1a). The grains of the α-Ti phase in the forged condition have irregular sizes and shapes. Smaller grains of the β-Ti phase are distributed along the grain boundaries of the α-Ti phase in the forged condition. Figure 1e shows the microstructure of the EBM condition, which is typically lamellar and parallel to the build direction (BD) [24,43]. In the EBMed sample, the α phase grew as lamellas and is surrounded by thinner lamellas of β phase.

Further details of the forged and EBMed microstructures can be observed by SEM (Fig. 1c,f) and line scans by EDS (Fig. 1d,g). In the forged condition, the smaller grains of the β-Ti phase are surrounding the grain boundaries of the matrix of α-Ti. Through the line scan, the distribution of the abovementioned α (Al) and β (V) stabilizers can be seen in both constituent phases. While the β-Ti phase is richer in V, the α-Ti phase possesses a higher content of Al. Moreover, compared to the forged condition, the lamellar morphology of the EBMed condition (Fig. 1f) shows a more homogeneous distribution of β-Ti through the microstructure. Compared with the forged condition (Fig. 1d), the line scan of the EBMed sample (Fig. 1g) shows a higher homogeneity in the alloy-elements content through both present phases. The more homogeneous distribution of alloying elements along the EBMed sample might be related to the lamellar morphology restraining the uneven distribution of alloying elements [28].

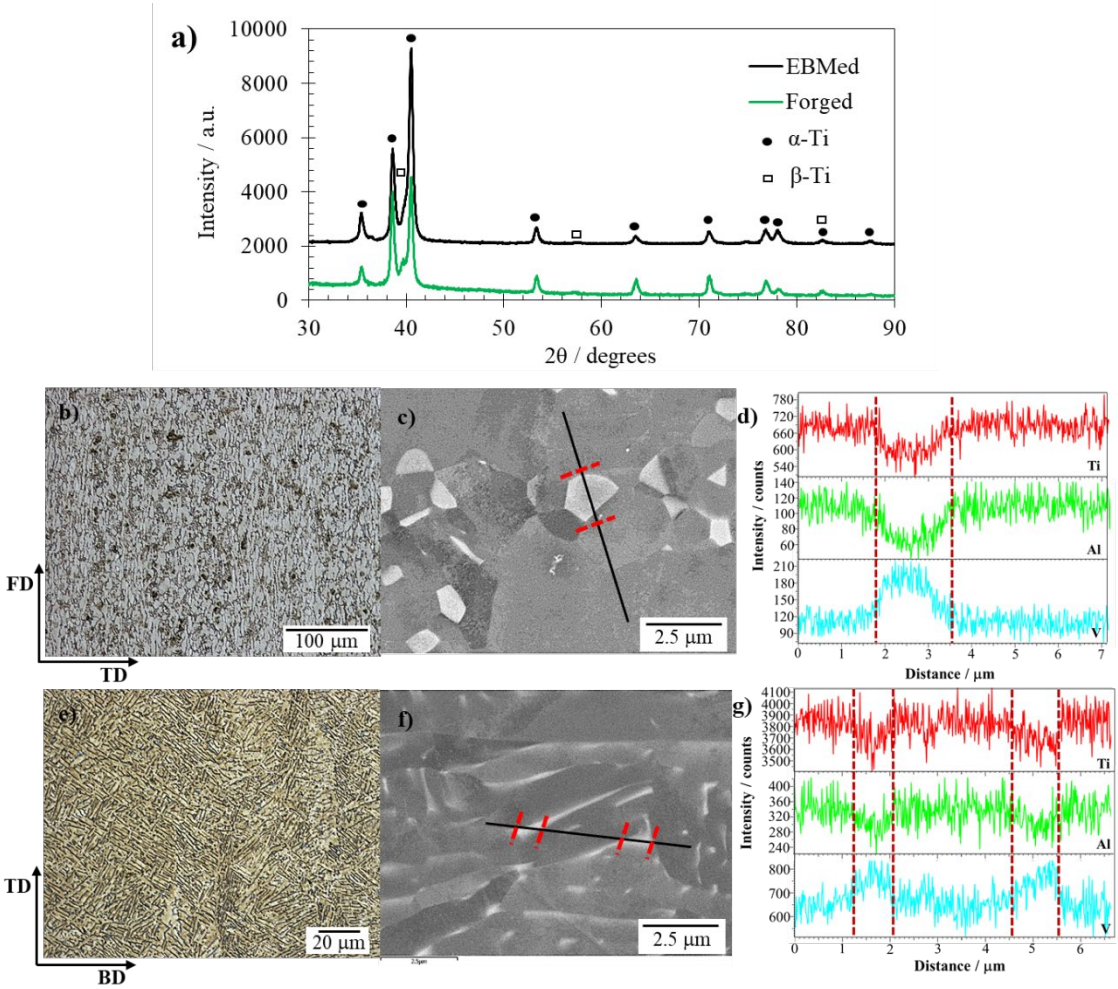

Figure 1. *Microstructural studies of the EBMed and forged conditions of the Ti-6Al-4V alloy by a) XRD patterns, b,e) OM, c,f) SEM, and d,g) line scan by EDS of b-d) forged and e-g) EBMed Ti-6Al-4V alloy conditions. FD, TD, and BD are forge, transversal, and build directions, respectively.*

To study the crystallographic texture of both conditions, Fig. 2 shows the orientation distribution functions (ODFs) calculated from EBSD analyses, as well as the simulated ones. Throughout the EBSD analyses, the α-Ti contents on forged and EBMed conditions were 95.4 and 95.0%, respectively. The rest corresponds to the β-Ti. Those contents of phases are congruent with the bigger area of α-Ti XRD peaks observed in Fig. 1.

The ODFs allow identifying the orientation density of crystalline planes. The coordinates of a given orientation are defined in terms of the three Euler angles, such given orientations are also called texture components. By the experimental intensity of the ODFs,

the density of preferred orientation crystal planes on the EBMed condition (Fig. 2c,d) is bigger than that for the forged one (Fig. 2a,b). It is well known that texture has a strong dependence on the thermo-mechanic history of material [44]. Thus, the different distribution of preferred oriented crystals between the forged and EBMed conditions was expected.

Figure 2a, b shows the experimental ODFs of the forged Ti-6Al-4V alloy for α-Ti. and β-Ti phases, respectively. Seven different texture components were identified on the α-Ti, while the other three on the β-Ti. The identification and Bunge notation in Euler angles (φ_1,Φ, φ_2) of the found main texture components are included in Table 1 (F_TC1 to F_TC10). Besides, in the EBMed condition (Fig 2c,d), seven and four different texture components were identified as E-TC1 to E-TC11 (Table 1) for the α-Ti and β-Ti phases, respectively. This means that both phases have a no-random distribution of crystal planes through the sample, and both studied conditions developed different crystallographic textures. As the texture strongly influences the surface energy, it is closely related to the mechanical, physical, and biological properties of Ti alloys [44–47]. Therefore, different properties can be expected between forged and EBMed conditions. It is noteworthy that the texture component, identified as F_TC8 in Table 1, is also widely reported as cube orientation on cubic crystal cells. The cube orientation is related to recrystallized grains on cubic materials as is the β-Ti phase [48]. The formation of the cube texture component could have resulted from the application of an annealing heat treatment after the forging. All of the abovementioned experimental main texture components (Fig. 2a,b,c,d) have an acceptable concordance with their simulations (Fig. 2a.1,b.1,c.1,d.1) of ideal texture components. This concordance shows a reliable level of confidence in the identified texture components of both conditions.

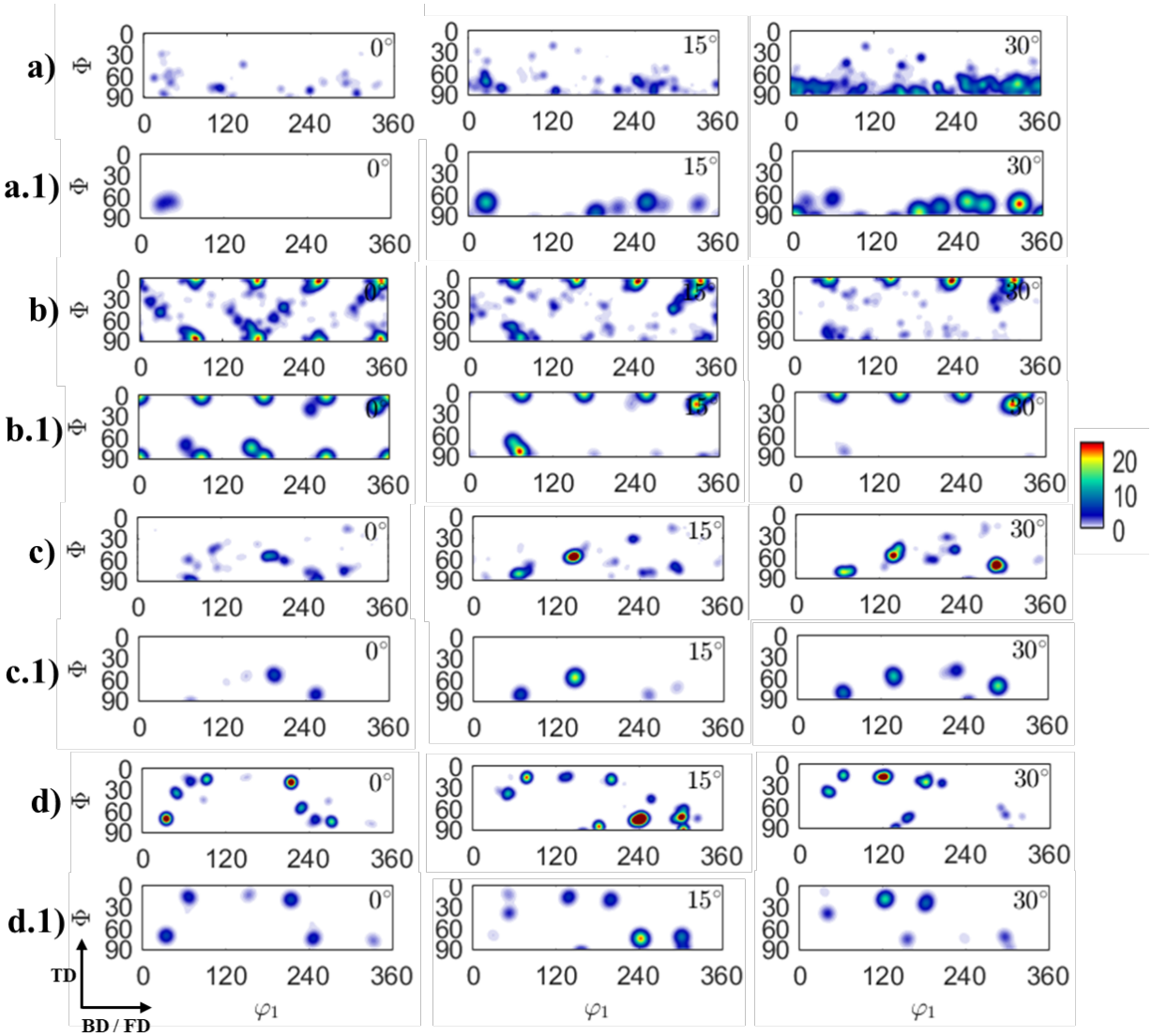

Figure 2. *Experimental orientation distribution functions (ODFs) of a,c) α-Ti and b,d) β-Ti for forged and EBMed conditions, respectively. Moreover, simulations of the identified ideal texture components for a.1,c.1) α-Ti and b.1,d.1) β-Ti for forged and EBMed conditions, respectively. TD, BD, and FD are transversal, build, and forged directions, respectively.*

Table 1. *Identified texture components on the forged and EBMed Ti-6Al-4V conditions.*

Condition	Phase	Texture component identification	Bunge notation angles			Fraction / %
			φ_1	Φ	φ_2	
Forged	α-Ti	F_TC1	326.3	74.8	32.7	7.5
		F_TC2	51.9	67.8	283.1	4.4
		F_TC3	182.4	86.9	146.1	6.2
		F_TC4	252.9	71.3	85.3	5.9
		F_TC5	276.5	76.4	92.1	4.6
		F_TC6	24.9	71.4	314.6	3.9
		F_TC7	212.6	79.5	148.8	3.3
	β-Ti	F_TC8	0.0	0.0	0.0	15.0
		F_TC9	157.0	80.0	70.0	11.8
		F_TC10	72.0	84.0	15.0	17.8
EBMed	α-Ti	E_TC1	143.1	569.0	200.3	16.9
		E_TC2	201.1	54.3	169.0	12.0
		E_TC3	66.2	81.7	263.3	10.9
		E_TC4	288.2	71.8	90.9	11.7
		E_TC5	224.0	49.6	157.1	5.0
		E_TC6	133.4	65.1	222.3	7.7
		E_TC7	254.0	82.0	5.0	4.9
	β-Ti	E_TC8	102.9	19.0	231.7	43.0
		E_TC9	168.9	25.5	224.3	19.7
		E_TC10	216.6	18.9	177.2	12.3
		E_TC11	45.7	38.7	293.0	8.4

To provide an insight into the role of the surface condition on bacterial proliferation, optical profilometry surface topography results are shown in Fig. 3. By a general overview of surface profiles, it can be seen higher maxima intensity along the scanned area for the EBMed condition (Fig. 3b) in comparison to the forged one (Fig. 3a). The parameters used to describe the roughness of both studied conditions of Ti-6Al-4V were included in Fig. 3c.

From the comparison between the area average roughness (S_a) and the root mean square roughness (S_q), the forged sample surface is slightly smoother than the EBMed condition. The slightly smoother profile of the forged sample was also observed by comparing the surface topography of forged and EBMed conditions (Fig. 3a,b). In both conditions, the surface roughness average values agreed with the reported roughness that allows an adequate staphylococcal bacterial adhesion [49]. However, it should be considered that S_a and S_q parameters indicate significant deviation from the arithmetical mean average height, but are insensitive in differentiating morphologies as peaks, valleys, as well as spacing between them. Due to the above, Sa and Sq do not give a complete description of the surface roughness. For further analysis, the skewness (S_{skw}) and the kurtosis (S_{kur}) parameters provide information about the static coefficient of friction by the height surface distribution [50]. A value of S_{kur} equal to 3 indicates a Gaussian surface height distribution; values of S_{kur} down to 3 suggest a surface with a homogeneous height distribution; and S_{kur} values greater than 3 are characteristic of narrow height distributions evident by sharp peaks [51]. Based on the above, the positive S_{kur} near to 3 and negative S_{skw} near to zero for the EBMed sample indicate a surface with a nearly Gaussian height distribution [50]. On the other hand, the positive values of S_{skw} and S_{kur} for the forged condition indicate turned surfaces with fairly high spikes that protrude above a flatter average, as well as numerous high peaks and low valleys, respectively [52].

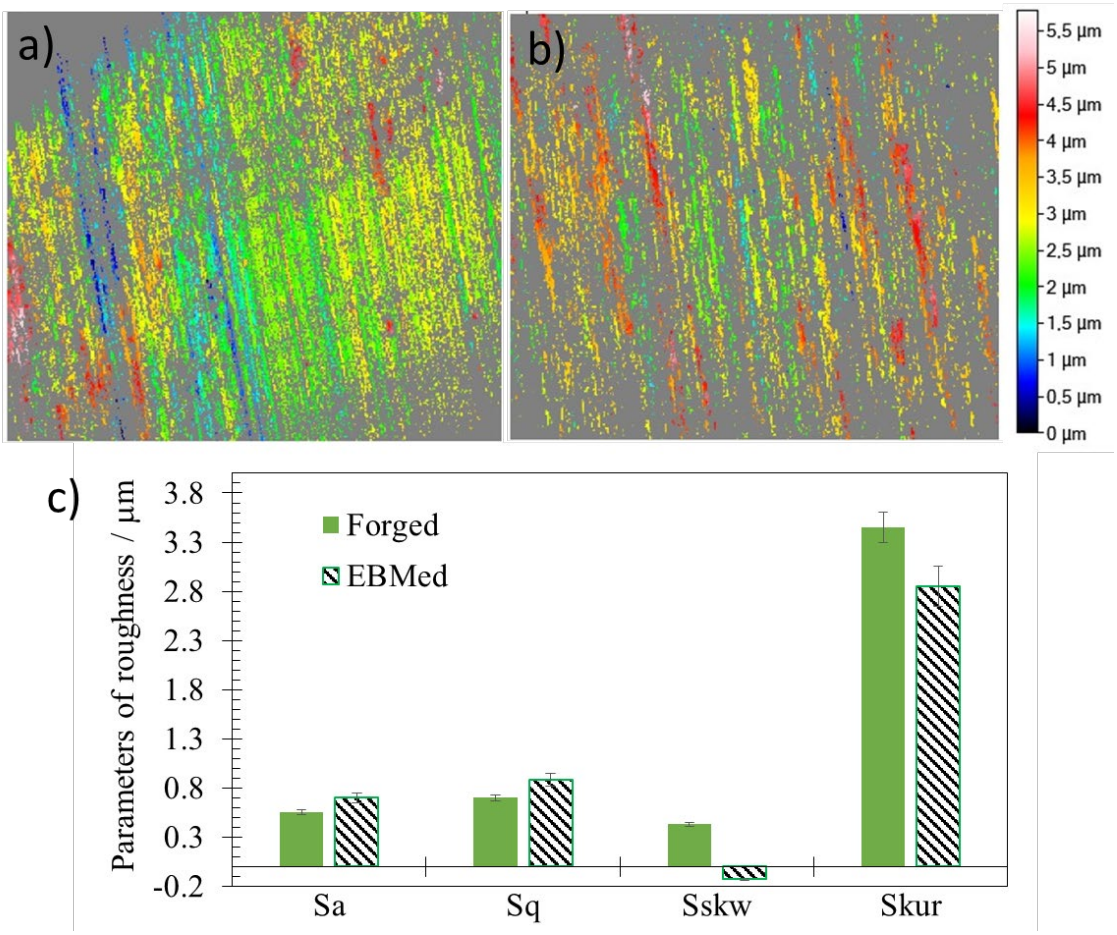

Figure 3. *Typical surface topography of a) forged and b) EBMed Ti-6Al4V alloy, as well as its c) optical profiling parameters to describe the surface roughness.* S_a, S_q, S_{skw}, *and* S_{kur}.

3.2. *Mechanical behavior*

To correlate the effect of microstructure on the mechanical behavior of forged and EBMed conditions, microhardness, tensile, and IET tests were carried out. Figure 4 shows the stress-strain curves of both studied conditions, which show similar elastic and plastic behaviors. Table 2 displays the main mechanical properties obtained for the forged and EBMed conditions. By comparing both conditions, the EBMed condition has ~8.8% and 7.2% higher YS and UTS values, respectively. Considering that both conditions have comparable α and β phases percentages (section 3.1), the slight change might be related to the difference in grain morphology. It has been reported that fine lamellar grain morphologies in Ti alloys, like the obtained in the EBMed condition, are related to higher

dislocation blocking capability and higher strengthening [22]. Furthermore, the smaller grain size in the EBMed sample implies grain boundary strengthening. Moreover, it is well-known that the β-Ti phase used to have superior mechanical strength at room temperature than the α-Ti phase [53,54]. Thus, compared to the forged condition, the slight increment in the content of the β phase in the EBMed condition could influence its slight increment in strengthening. Additionally, the occurrence of hetero-deformation induced (HDI) strengthening due to possible strain gradients between the soft (α-Ti) and hard (β-Ti) phases [55,56] cannot be denied in both conditions. The HDI strengthening has shown important contributions in other Ti-heterostructured alloys [57]. However, the mechanical incompatibility between both phases should be greater than 100% to obtain a significant effect of HDI strengthening [58]. The Ti-6Al-4V alloys have shown values of YS from about 760 to 860 MPa in the β-type and of about 1030 MPa in the α-type [54]. Therefore, the HDI strengthening contribution could be neglected.

Moreover, the obtained UTS value in the EBMed sample (1024.0 MPa) was higher than those for selective laser melted (SLM) Ti-6Al-4V in hot-rolled (968 MPa) and dense core with a porous surface (989 MPa) [59]. Additionally, the E value of the EBMed sample (106.5 MPa) was smaller than the obtained for SLMed conditions from tensile tests, which were 117.2 MPa for the hot-rolled; and 118.9 GPa for the dense core with a porous surface [59]. This difference is related to the superior precision of measuring E by dynamic methods, such as the IET technique, compared to mechanical tests [60]. This statement agrees with the room temperature E values of Ti-6Al-4V from ~105 to 109 GPa and 113 to 114 GPa obtained by IET [61,62] and tensile tests [63,64], respectively. Regarding the YS values of EBM (980 MPa) and forge (900 MPa) obtained samples, both are higher than the YS values reported for bones, which range from 104 to 121 MPa [65]. For last, the microhardness of both studied conditions (from 293.3 to 294.6 $HVN_{0.3}$) was comparable to that of fully annealed Ti-6Al-4V ($HVN_{0.2}$=287.8) [66]. The hardness of both conditions (about 2876 to 2889 MPa) was up to the minimum hardness reported for osteonal, interstitial, and trabecular bone regions (230 to 760 MPa) [67]. From the above, the tensile and hardness properties met the mechanical requirements of the bone.

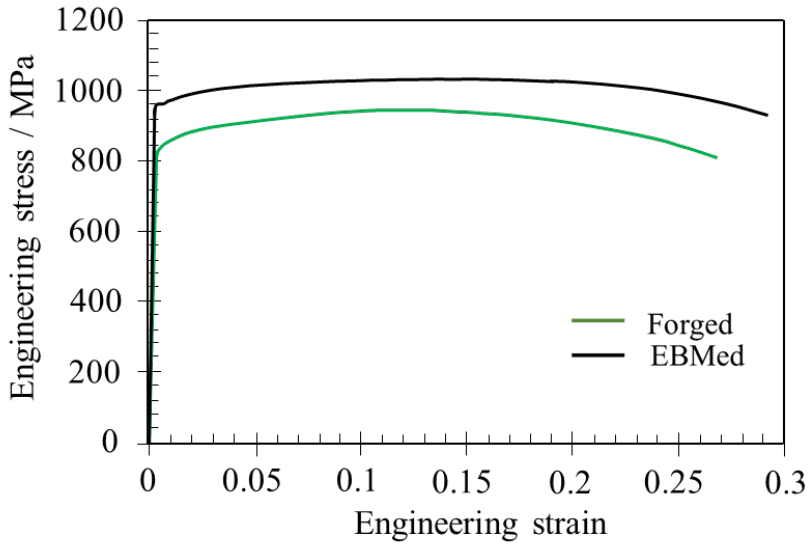

Figure 4. *Tensile stress–strain curves for the forged and EBMed Ti-6Al-4V alloys.*

Table 2. *Mechanical properties of forged and EBM Ti-6Al-4V alloys.*

Sample	**$HVN_{0.3}$**	**E / GPa**	**YS / MPa**	**UTS / MPa**
Forged	294.6 ± 39.0	105.9 ± 1.6	900.0 ± 20.0	955.0 ± 37.0
EBMed	293.3 ± 15.0	106.5 ± 1.9	980.0 ± 11.0	1024.0 ± 33.0

3.3.*Ion release measurement*

Ion release measurements are critical to the study of biomaterials because metal ions can play an important role in health when they diffuse into the human body. Large amounts of released metal ions can accumulate in the organs, as well as cause allergy and carcinoma [68]. The concentrations of Ti, Al, and V ions released from the forged and EBMed alloys in artificial saliva are shown in Fig. 5. In comparison with the forged alloy, the EBMed condition released greater concentrations of the three main elements of the Ti-6Al-4V alloy. Nonetheless, the Ti ion release for forged and EBMed conditions (3268.4 to 3787.8 $\mu g/cm^2\ L^1$, respectively) was quite below the estimated dietary intake of Ti of 0.88 mg/day [69]. The Al ion release from both conditions (between 271 to 350 $\mu g/cm^2\ L^1$) is below the provisional tolerable weekly intake (PTWI) of 2 mg/kg body weight [70]. The Al ion

release is also lesser than the mean Al content in some common foods like rice (1.5 mg/kg), butter (2.1 mg/kg), nuts (4.7 mg/kg), among others [71]. The V content was also into the estimated daily intake of this element, which is 10.36 μg/day [69].

It is also worth mentioning that the main source of ion release is the corrosion process that occurs between the biomaterial and oral fluids [72]. The metal ions released are directly related to the passive film regeneration time, i.e., the longer the restoration time, the greater the diffusion of the ions. The Ti-6Al-4V alloy was reported with less passive film regeneration time in comparison to other biomaterials as SUS316L, Co-28Cr-6Mo, and Zr-2.5Nb [73]. According to Okazaki and Gotoh [74], titanium alloys exhibit low ion release rates due to their high corrosion resistance, which is strongly affected by the corrosive medium and by decreasing pH. However, the body's extracellular fluid is a buffered solution that retains a pH between 7.35 and 7.45 [75]. Due to this, the drop in pH in hard tissue with an implant (down to ~5.2) recovers to a value of 7.4 within two weeks [76].

To discern the microstructural changes generated by the corrosive medium of artificial saliva, Fig. 5b,c shows the OM micrographs obtained for the forged and EMBed materials after testing. The effect of artificial saliva is evident in all samples since it delimited the grain boundaries, in addition to preferentially attacking the grains of the β-Ti phase shown as the darkest areas. The preferential etch of the β-Ti phase in both Ti-6Al-4V conditions was expected due to compositional changes compared to the matrix [77,78]. Such chemical gradients in the β-Ti phase were shown in Fig. 1. Likewise, the EBMed alloy was the most etched by the medium (Fig. 5c), which is congruent with the higher level of ions release, showed in Fig. 5a. Considering that, both conditions have similar percentages of phases and similar smooth surface roughness (due to metallographic preparation), the higher ion release on the EBMed sample could be related to the differences in crystallographic texture. As surface energy plays an important role in the corrosion susceptibility of metallic materials, the surface energy of texture components might be related to the ion release behaviors. Due to the β-Ti was the most active phase during the corrosion process, only the texture components of this phase were considered. The expressions on Miller notation for the texture components of β-Ti phase for both studied materials are shown in Table 3. It has been reported that corrosion susceptibility is

strongly influenced by the crystallographic planes which are located parallel to the surface exposed to the corrosive environment. The planes with higher atomic densities (compaction) show less corrosion susceptibility due to their lower surface energy [79]. Due to none of the texture components coincided with the well-known slip systems in bcc structures (most compacted planes), i.e., {110}<111>, {112}<111> and {123}<111>, it was suggested that the texture on β-Ti phase on both alloys contribute to the increment of corrosion rate. Moreover, the higher relative fraction of texture components (Table 1) on the EBMed sample, might be related to the higher ion release.

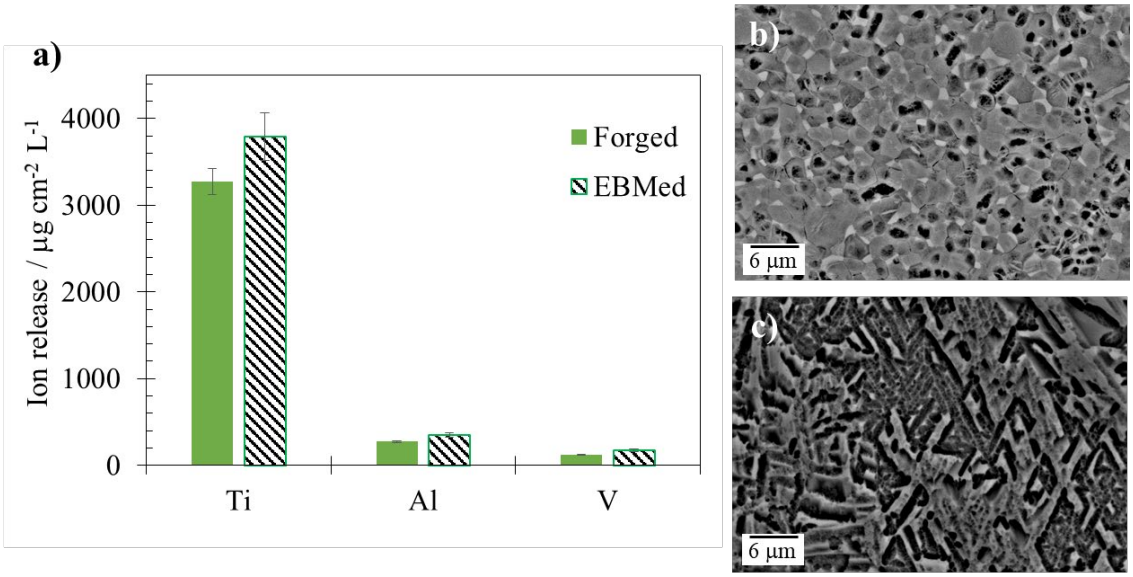

Figure 5. *a) Concentration of the released Ti, Al, and V for the forged and EBMed conditions and OM micrographs after the ion release tests on b) forged and c) EBMed Ti-6Al-4V alloy.*

Table 3. *Texture components of β-Ti phase in Miller notation for forged and EBMed materials.*

Condition	**Identification of texture component**	**Family of planes**	**Family of directions**
Forged	F_TC8	{001}	<100>
	F_TC9	{931}	<383>
	F_TC10	{391}	<329>
EBMed	E_TC8	{114}	<311>

	E_TC9	{339}	<851>
	E_TC10	{2 32 95}	<83 52 19>
	E_TC11	{528}	<844>

3.4. Corrosion behavior

Figure 6a presents the open circuit potential (OCP) graphs of the forged and EMBed materials, along with immersion in 1M NaCl. In both conditions, the initial values of OCP showed negative values, indicating that the ground base alloy was active. The corrosion potential increased in the primary immersion stage; and then, remained almost constant from the 80 s immersion time. Both conditions stabilized at similar electrochemical potentials. The OCP values stabilized quickly enough, which indicates efficient passive oxide layer formation. It is noteworthy that, higher OCP values at the steady-state were obtained for both studied conditions compared to Ti-1300 and equiaxed Ti-6Al-4V alloys [78], implying the formation of a more stable surface oxide layer.

The suggestion of passive layer formation was corroborated by the potentiodynamic (PD) curves (Fig. 6b) of the forged and EBMed conditions. Both materials showed similar polarization behavior. After cathodic polarization, all the samples revealed superficial passivation, as indicated by the nearly constant current densities with incremented potential up to ~1.4 V. The relevance of this passive layer lies in protecting the material surface from corrosion, which occurs when the oxide film is damaged by coming into contact with other oral environment components [80]. The passivation current densities of EBMed and forged conditions were about $1.0x10^{-5}$ and $9.8x10^{-6}$ $\mu A \cdot cm^{-2}$, respectively, which suggests lower corrosion resistance for the EBMed alloy. However, up to 1.4 V, both curves showed transition at the passivation region by slightly increasing their current density. This could imply the presence of microgalvanic interactions, especially in the EBMed sample, which showed a peak of current density at about 1.9 V. This peak is related to pitting corrosion generation due to breakage of the oxide surface layer [78]. This is, the Cl- ions penetrated the oxide film down to the Ti-6Al-4V substrate and assist in the dissolution reactions at the substrate/oxide interface.

Pitting corrosion is a common phenomenon reported for the Ti-6Al-4V subjected to NaCl solution [30]. It has been reported that the type, size, and morphology of phases

strongly influence the electrochemical behavior of the Ti-6Al-4V [30]. Considering both samples have similar phases content (~95% of α phase and rest of β phase), the grain size and morphology might play a key role in the electrochemical response of the studied materials. Small grain size and lamellar morphology of the Ti-6Al-4V, similar to the obtained in the EBMed sample, were reported with lower pitting potential (E_{pit}) in 3.5 wt.% NaCl than coarser and equiaxed morphologies (similar to that of the forged sample) [30]. As the E_{pit} refers to the potential above which nucleation and growth of pits occur, the low E_{pit} expected for the EBMed condition of this study might be related to the pitting formation, not so for the forged condition.

Table 4 shows the electrochemical parameters obtained by the PD curves of both studied conditions. It should be noted that the CR from Table 4 is related to the occurrence of uniform or general corrosion rather than localized (pitting) corrosion [81]. Uniform corrosion is characterized by degradation of material at about the same rate over the whole studied surface due to cathodic and anodic zones being randomly located through the microstructure [81]. From Table 4, the electrochemical parameters of corrosion current density (i_{corr}) and corrosion potential (E_{corr}) are higher in the EBMed sample compared to the forged one. Consequent lower polarization resistance (Rp) and higher corrosion rate (CR) were also obtained in the EBMed sample. The more negative Ecorr in the EBMed sample is related to a higher number of active sites for corrosion [82]. Comparing the E_{corr} of the EBMed Ti-6Al-4V (E_{corr} = -0.43) with other reported Ti systems as Ti–35Nb produced by SLM, as well as rolled and SLMed Ti-6Al-4V in 3.5 wt.% NaCl (~-0.47 < E_{corr} > -0.55 V), the EBMed condition suggested a higher corrosion resistance [30,83]. Moreover, the lower corrosion rates are related to lower corrosion current densities [30], being congruent with the lower CR in the forged sample compared to the EBMed condition. However, fine and lamellar grain morphologies (like the obtained by EBM) are reported with better uniform corrosion resistance than coarse and equiaxed morphologies (similar to that obtained by forge) in 3.5 wt.% NaCl [30]. The results of Table 4, apparently contradictory to the literature, can be explained in terms of crystallographic texture. As explained in Table 3, the crystallographic planes in the β phase (the preferred etched phase), as well as the higher texture intensity in the EBMed sample (Table 1), could increase the surface energy of the EBMed condition. This means that the surface energy of

the β phase in the EBMed sample compared to the forged one, might be higher and encourage the corrosion processes. From the above, the electrochemical results agree with the results obtained from Fig. 5. For both studied conditions, the corrosion rates are lower than the maximum recommended by the American Association of Corrosion Engineers of 0.05 mm/year [29]. Furthermore, the corrosion resistance ($\leq 10^{-3}$ mm year^{-1}) allows considering both conditions as highly stable [30].

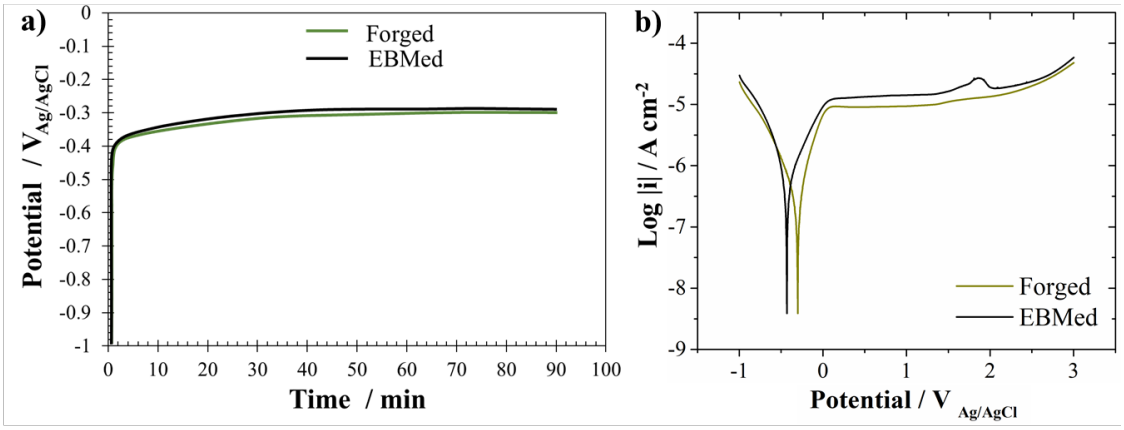

Figure 6. *a) Open circuit potential (OCP) and b) potentiodynamic (PD) curves of forged and EBMed alloys.*

Table 4. *Electrochemical parameters from potentiodynamic (PD) curves of both studied conditions.*

Condition	**E_{corr} (V)**	**i_{corr} (μA/cm^2)**	**Rp (kΩ)**	**CR (μm/year)**
EBMed	-0.43 ± 0.02	0.21 ± 0.04	367.81± 40.12	1.83 ± 0.13
Forged	-0.30 ± 0.02	0.11 ± 0.03	730.10 ± 57.41	0.91 ± 0.05

3.5. Biological effect triggered by materials in contact with MG63 cells

In the analysis of cytotoxicity obtained by the MTS assay (Fig. 7a-d), the cells treated with the conditioned medium for 24 hours did not present toxicity in the forged condition compared to the control group (P> 0.05). After seven days of treatment, the absorbance value increased from 0.4 to approximately 0.6, indicating that this conditioned medium did not promote harmful cellular metabolic alterations. This increase in the absorbance value also occurred for the control group (absorbance > 0.6). Such increment was related to the cell proliferation that occurred between 24h and seven days of the experiment, indicating that the cells continue proliferating. Compared to the control group, the Forged group in both 24h and seven days did not present a statistical difference. It is noteworthy that the MTS salt reacts with the enzymes present in the mitochondria of the cells, that is, only with the cells that show metabolic activity. The cells treated with the conditioned medium obtained by EBM, on the other hand, did not present cytotoxicity in 24 hours, compared to the control group, but the absorbance was higher for both groups, control and treated compared to values obtained in Fig. 7a. After seven days of treatment with this conditioned medium, the treated group showed a higher absorbance value (absorbance > 0.6) compared to the control group (absorbance > 0.4) (P<0.05). From these results, the medium conditioned in both studied conditions did not promote harmful effects either in short or long-term contact with the cells. Furthermore, the EBMed condition showed better biocompatibility than the forged condition after seven days of treatment.

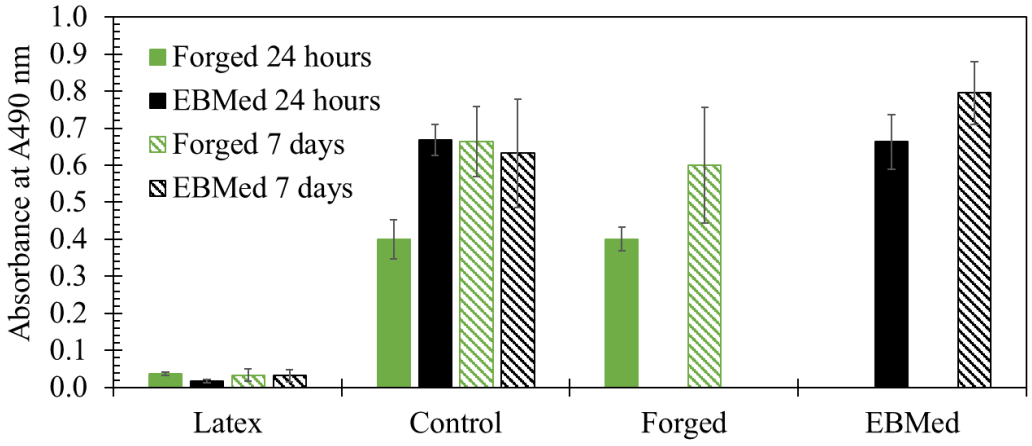

Figure 7. *Viability of the MG63 in contact with the conditioned medium for 24 hours and seven days for the forged and EBMed conditions.*

Figure 8 shows the adhesion of cells to the plate surfaces (control) and the materials obtained by forge and EBM. After 5 hours, the cells on the studied surfaces did not show significant cell adhesion compared to the control group in both materials (Fig. 8a,b,e,f). After 72 hours, there was significant cell proliferation on the material surfaces (Fig. 8d, h) compared to their respective controls (Fig. 8c,g). This was confirmed by staining (with eosin dye) in red the cytoplasm of the cells and staining (with DAPI dye) in blue the nuclei. It was observed that the cells promoted the connection with neighboring cells, through cytoplasmic projections indicated by the white arrows in Fig. 8d,h. These projections promoted a bridge between the cells that favored the cell adhesion process. The EBMed condition promoted a more attractive surface for cell proliferation compared to the forged condition. This was observed by the staining of the nucleus (cells with greater metabolic activity), represented by Fig. 8h. The mechanism of the cell-substrate interaction and the resulting morphology in this present work is consistent with the literature for different Ti alloys [84,85]. Cell proliferation is a sign of the nontoxicity and cytocompatibility of titanium alloys [85]. In this study, the nontoxicity was confirmed after 72 h.

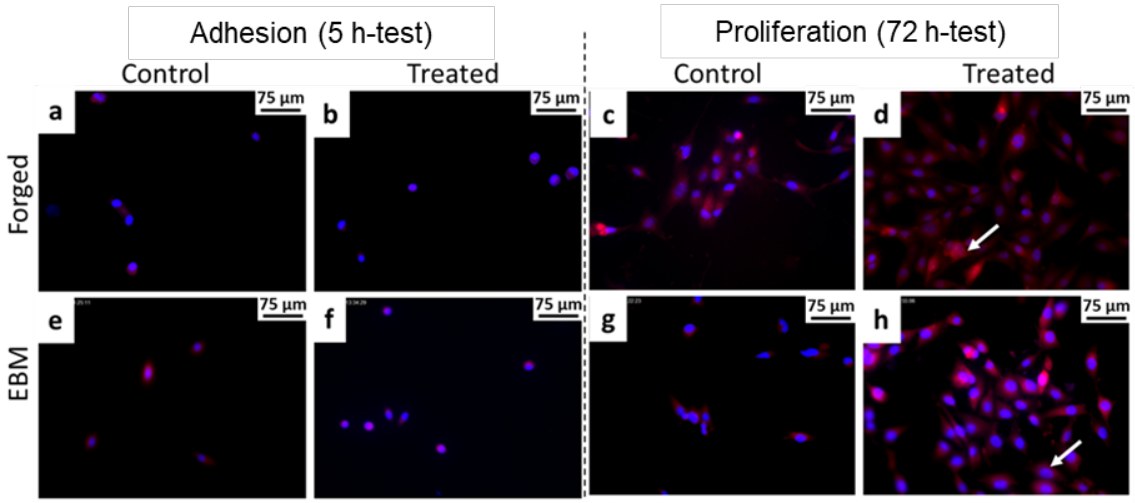

Figure 8. *Fluorescence analysis of MG63 adhesion and proliferation in contact with the surface of the materials after 5 and 72 hours for a-d) forged and e-h) EBMed condition.*

Table 5 shows the statistical quantification of adhesion and proliferation of cells for the forged and EBMed conditions. The confocal micrographs shown in Fig. 8 were

considered within the statistical sampling. The adhesion of cells was slightly higher in the EBMed material compared to the forge done. After 72 hours, both materials presented a significant increase in MG63 proliferation. The quantification of cells indicated that the proliferation process was more significant on the surface of the EBMed condition compared to the forged one. The energy expenditure is indeed higher during the cell proliferation process, causing the adhesion to be lower. Systematic reviews conducted by Teughels et al. and Truong et al. indicated that surface roughness has a strong effect on the bacterial attachment [86,87]. Moreover, roughness can influence the relationships between surface free energy and cell proliferation [88]. According to the previous analysis of surface roughness (Fig. 3), the higher adhesion of cells on the EBMed condition agreed with its higher Sa value compared to that of the forged sample.

Table 5. *Quantification of adhesion and proliferation of cells according to the specific control for each Ti-6Al-4V studied condition.*

Condition	**Parameter**	**Ratio (cells/cm^2)**
Forged	Adhesion (t=5h)	1.60±0.01
	Proliferation (t=72h)	2.85±0.02
EBMed	Adhesion (t=5h)	1.75±0.01
	Proliferation (t=72h)	3.75±0.06

3.6. Biofilm formation on different materials

The evaluation of biofilm formation of S. aureus and S. epidermidis on the forged and EBMed Ti6Al4V samples is shown in Fig. 9a. It is necessary to highlight that the size of the sample (n=9) promotes a high dispersion of the values, making it impossible to carry out inferential statistical tests. The average values of viable adhered S. aureus and S. epidermidis cells were greater in the sample obtained by EBM (1.54E+07 and 1.28E+07

CFU/cm^2) in comparison to the forged sample (1.30E+07 and 1.07E+07 CFU/cm^2). However, these differences were not statistically significant.

According to the literature, hydrophobic surfaces have higher bacterial colonization than hydrophilic ones. This phenomenon occurs because bacteria have to compete with water to adhere to hydrophilic surfaces [89]. However, other studies indicate that parameters such as chemical composition, wettability, and surface tension influence colonization on mainly polished surfaces. It has also been reported that roughness above 0.2 μm takes a determining role in the proliferation and adhesion of bacteria, displacing the other variables to a secondary role [86,88,90]. Szymczyk-Ziółkowska et al. analyzed the surface tension and contact angle of samples obtained by EBM [91]. Manufacturing, machining, sandblasted, and etched surfaces were compared in that study. They found that an increase in roughness (Sa) translates into an increase in the contact angle (hydrophobicity). This occurs due to small air pockets formation that alters the intermolecular interactions between the solid phase (material) and the liquid phase (internal medium). Therefore, higher roughness would lead to greater bacterial colonization. Likewise, for the S. aureus colonization test, they obtained that higher roughness translated into higher CFU values. Their CFU values (~10^7) in the samples after as-built were similar to those of the present work. In this study, the results of the optical profilometry of the forged sample (Fig. 3) indicated a profile with peaks along the surface. However, the peaks are distributed with higher homogeneity through the sample in comparison with the peaks and valleys on the EBMed condition. This could lead to the appearance of small air pockets that might increase the surface hydrophobicity and, therefore, increase the S. aureus bacterial colonization in the EBMed sample. Likewise, other authors observed a higher concentration of S. epidermidis in Ti-6Al-4V surfaces with higher Sa values [92]. Therefore, the literature agrees with the results of this study because the EBMed condition showed higher Sa and higher colonization by S. epidermidis and S. aureus. Moreover, considering the bactericidal properties of Al [93,94] and its heterogeneous distribution through the forged sample (Fig. 1), it might contribute to the decrement of S. epidermidis.

Figure 9b-e shows the micrographs of the surface of the samples obtained by forge and EBM after being colonized by S. epidermidis and S. aureus. The differences in the colonization pattern between both materials were observed. The S. epidermidis colonies in

all surfaces were homogeneous while the S. aureus colonies presented localized smoother layers of bacteria indicated in Fig. 9d,e with white arrows.

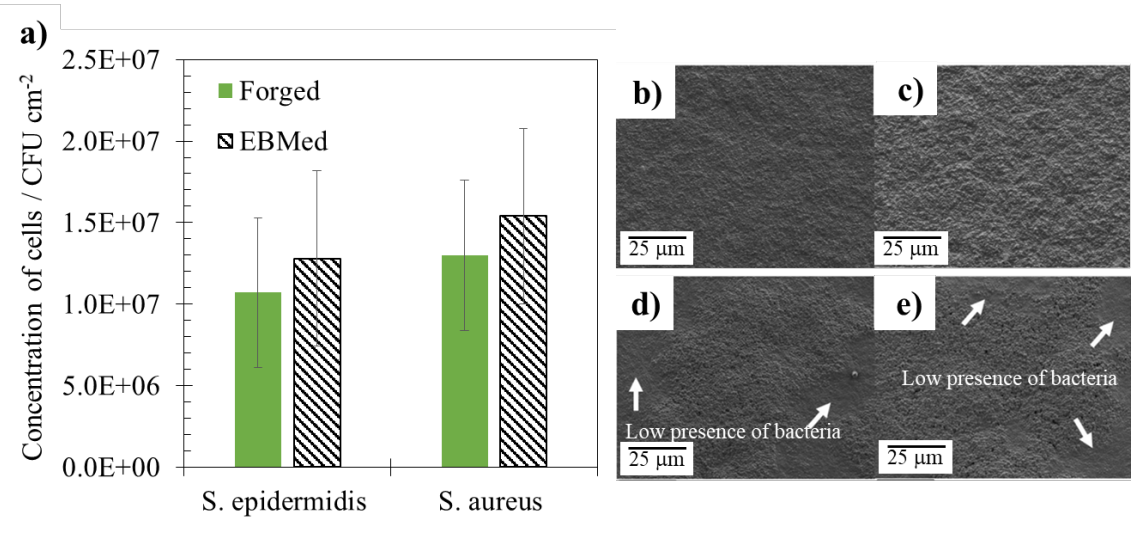

Figure 9. *a) Average number of viable adhered S. aureus and S. epidermidis cells in forged and EBMed conditions, as well as micrographs obtained by secondary electrons in b,d) forged and c,e) EBMed samples colonized by b,c) S. epidermidis d,e) and S. aureus.*

Figure 10 shows the surfaces of Ti6Al4V obtained by forged colonized by S. epidermidis and S. aureus. While the S. epidermidis adopted a rounded and more compacted shape, the S. aureus grew in like-grape clusters leaving some gaps between them. The white arrows in Fig. 10b and the magnification of Fig. 10c pointed to the bacteria during binary fission, i.e, the active bacteria asexual reproduction, indicating the active biofilm formation. The forged sample was selected as a reference due to similar morphologies of bacteria were obtained in the EBMed sample.

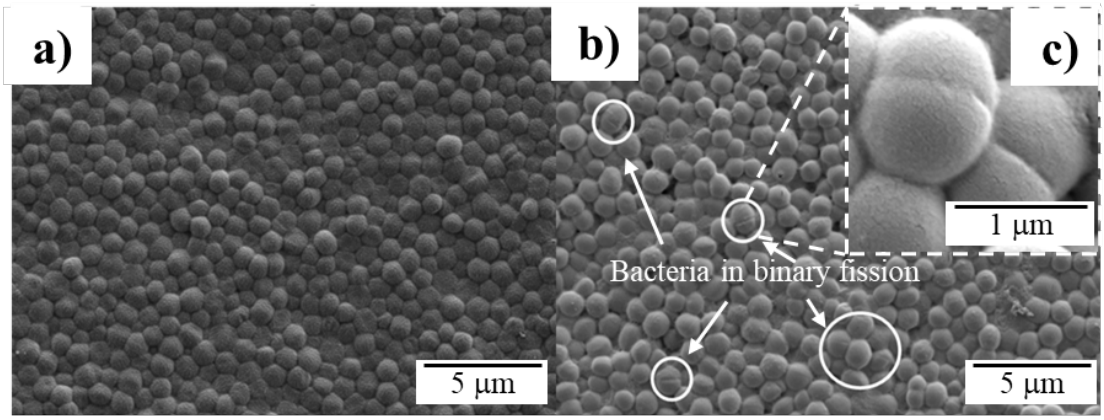

Figure 10. *SEM micrographs by a secondary electron detector of the forged Ti6Al4V surface colonized by a) S. epidermidis and b) S. aureus, as well as c) magnification of the bacterial binary fission of S. aureus.*

In summary, as the phases content is similar between the forged and EBMed conditions, it did not play an important role in the mechanical, ion release, electrochemical, or in-vivo biological tests carried out in this work. The grain morphology and size strongly affected the strengthening mechanisms of the studied materials. The lamellar morphology and smaller grains of the EBMed alloy could prompt the dislocation blocking capability and grain boundary strengthening compared to the forged condition. As result, the EBMed condition showed a slight increment on YS and UTS compared to the forged material. The behavior of the Ti-6Al-4V alloy in different corrosive media as 3.5 wt.% NaCl and artificial saliva was strongly influenced by its crystallographic texture. In both, forged and EBMed conditions, the β phase was preferentially etched due to its V enrichment. Thus, the β phase degradation controlled the corrosive processes in both materials. The higher intensity of crystalline planes oriented in directions different to those with the lower surface energy could cause the higher ion release and corrosion rates in the EBMed condition. However, only the EBMed sample showed local corrosion tendency in the PD curves, which might be related to microgalvanic interactions encouraged by the lamellar morphology of the EBMed condition. For last, the surface roughness played a decisive role in the in-vivo biological assessment in both alloys. The adhesion and proliferation of cells, as well as the biocompatibility, were higher in the alloy with higher Sa. The higher biofilm formation in the EBMed sample could be related to the increment of hydrophobicity due to its higher Sa

value. The heterogeneous distribution of Al along the forged sample could also contribute to the decrement of the S. epidermidis proliferation.

4. Conclusions

The microstructural and surface characteristics of forged and EBMed Ti-6Al-4V alloy were correlated to their mechanical, corrosion, and biological behaviors. The main conclusions are summarized as follows:

1. The EBMed condition showed slightly higher mechanical properties (YS and UTS) than the forged condition. This was related to the smaller grain sizes and the higher dislocation blocking capability of the lamellar morphology in the EBMed condition compared to the coarse forged microstructure. The tensile and hardness properties met the mechanical requirements of the human bone.
2. The EBMed sample showed higher ion release and electrochemical corrosion rates than the forged condition. This could be related to the effect of higher density of preferred oriented grains in planes that do not correspond to the ones with lower surface energy in the β phase. However, both studied conditions showed ion release rates below the estimated dietary intake and highly stable corrosion rates.
3. The higher area average surface roughness (Sa) of the EBMed condition prompted its higher biocompatibility, as well as higher adhesion and proliferation of cells. None of the Ti-6Al-4V conditions indicated harmful effects in either the short or long term.
4. Both studied conditions of the Ti-6Al-4V are feasible candidates for dental and orthopedic implants. However, the forged condition is more recommended for patients with clinic stories related to S. epidermidis and S. aureus illnesses.

Acknowledgments

This work was supported by Ministerio de Economía y Competitividad from Spain under the RTI2018-097810-B-I00 grant number and by the European Commission through FEDER. L. R-R. acknowledges CONACYT for the scholarship granted under the number 465504. Valuable technical support provided by Rafael Ibarra-Contreras is also acknowledged.

Data Availability

The raw data related to this manuscript would be made available on request.

References

[1] M. Geetha, A.K. Singh, R. Asokamani, A.K. Gogia, Ti based biomaterials, the ultimate choice for orthopaedic implants - A review, Prog. Mater. Sci. 54 (2009) 397–425. https://doi.org/10.1016/j.pmatsci.2008.06.004.

[2] M. Bahraminasab, B.B. Sahari, K.L. Edwards, F. Farahmand, M. Arumugam, T.S. Hong, Aseptic loosening of femoral components - A review of current and future trends in materials used, Mater. Des. 42 (2012) 459–470. https://doi.org/10.1016/j.matdes.2012.05.046.

[3] B.G. Pound, Corrosion behavior of metallic materials in biomedical applications. I. Ti and its alloys, Corros. Rev. 32 (2014) 1–20. https://doi.org/10.1515/corrrev-2014-0007.

[4] S.L. Sing, J. An, W.Y. Yeong, F.E. Wiria, Laser and electron-beam powder-bed additive manufacturing of metallic implants: A review on processes, materials and designs, J. Orthop. Res. 34 (2016) 369–385. https://doi.org/10.1002/jor.23075.

[5] Y. Okazaki, T. Tateishi, Y. Ito, Corrosion resistance of implant alloys in pseudo physiological solution and role of alloying elements in passive films, Mater. Trans. 38 (1997) 78–84. https://doi.org/https://doi.org/10.2320/matertrans1989.38.78.

[6] R.J. Solar, S.R. Pollack, E. Korostoff, In vitro corrosion testing of titanium surgical implant alloys: An approach to understanding titanium release from implants, J. Biomed. Mater. Res. 13 (1979) 217–250. https://doi.org/10.1002/jbm.820130206.

[7] Y. Nakayama, T. Yamamuro, Y. Kotoura, M. Oka, In vivo measurement of anodic polarization of orthopaedic implant alloys: comparative study of in vivo and in vitro experiments, Biomaterials. 10 (1989) 420–424. https://doi.org/10.1016/0142-9612(89)90134-8.

[8] D.C. Hansen, The Effect of a Novel Biopolymer on the Corrosion of 316L Stainless Steel and Ti6Al4V Alloys in A Physiologically Relevant Electrolyte, Corrosion.

(2007).

[9] K.M. Speck, A.C. Fraker, Anodic Polarization Behavior of Ti-Ni and Ti-6A 1-4 V in Simulated Physiological Solutions, J. Dent. Res. 59 (1980) 1590–1595. https://doi.org/10.1177/00220345800590100601.

[10] A. Choubey, R. Balasubramaniam, B. Basu, Effect of replacement of V by Nb and Fe on the electrochemical and corrosion behavior of Ti-6Al-4V in simulated physiological environment, J. Alloys Compd. 381 (2004) 288–294. https://doi.org/10.1016/j.jallcom.2004.03.096.

[11] A. Mitchell, Melting, casting and forging problems in titanium alloys, Mater. Sci. Eng. A. 243 (1998) 257–262. https://doi.org/10.1016/s0921-5093(97)00810-1.

[12] H.B. Bomberger, F.H. Froes, The Melting of Titanium, J. Met. 36 (1984) 39–47.

[13] G. Ghazal, P. Chapelle, A. Jardy, J. Jourdan, Y. Millet, Dissolution of high density inclusions in titanium alloys, ISIJ Int. 52 (2012) 1–9. https://doi.org/https://doi.org/10.2355/isijinternational.52.1.

[14] A. Mitchell, D.W. Tripp, HID and HDI dissolution during titanium melting processes, (1993) 2257–2264.

[15] L.E. Murr, S.A. Quinones, S.M. Gaytan, M.I. Lopez, A. Rodela, E.Y. Martinez, D.H. Hernandez, E. Martinez, F. Medina, R.B. Wicker, Microstructure and mechanical behavior of Ti-6Al-4V produced by rapid-layer manufacturing, for biomedical applications, J. Mech. Behav. Biomed. Mater. 2 (2009) 20–32. https://doi.org/10.1016/j.jmbbm.2008.05.004.

[16] A. Saboori, D. Gallo, S. Biamino, P. Fino, M. Lombardi, An overview of additive manufacturing of titanium components by directed energy deposition: Microstructure and mechanical properties, Appl. Sci. 7 (2017). https://doi.org/10.3390/app7090883.

[17] W.E. Frazier, Metal additive manufacturing: A review, J. Mater. Eng. Perform. 23 (2014) 1917–1928. https://doi.org/10.1007/s11665-014-0958-z.

[18] S. Ponader, C. Von Wilmowsky, M. Widenmayer, R. Lutz, P. Heinl, C. Körner, R.F.

Singer, E. Nkenke, F.W. Neukam, K.A. Schlegel, In vivo performance of selective electron beam-melted Ti-6Al-4V structures, J. Biomed. Mater. Res. - Part A. 92 (2010) 56–62. https://doi.org/10.1002/jbm.a.32337.

[19] G.A.W. Murray, J.C. Semple, Transfer of Tensile Loads from a Prosthesis to Bone Using Porous Titanium, J. Bone Jt. Surg. 63B (1981) 138–141. https://doi.org/10.1302/0301-620X.63B1.7204467.

[20] M. Bram, T. Ebel, M. Wolff, A.P.C. Barbosa, N. Tuncer, Applications of powder metallurgy in biomaterials, Adv. Powder Metall. (2013) 520–554. https://doi.org/10.1533/9780857098900.4.520.

[21] T.S. Goia, K.B. Violin, M. Yoshimoto, J.C. Bressiani, A.H.A. Bressiani, Osseointegration of Titanium Alloy Macroporous Implants Obtained by PM with Addition of Gelatin, Adv. Sci. Technol. 76 (2010) 259–263. https://doi.org/10.4028/www.scientific.net/ast.76.259.

[22] X. Zhao, S. Li, M. Zhang, Y. Liu, T.B. Sercombe, S. Wang, Y. Hao, R. Yang, L.E. Murr, Comparison of the microstructures and mechanical properties of Ti-6Al-4V fabricated by selective laser melting and electron beam melting, Mater. Des. 95 (2016) 21–31. https://doi.org/10.1016/j.matdes.2015.12.135.

[23] K.C. Nune, S. Li, R.D.K. Misra, Advancements in three-dimensional titanium alloy mesh scaffolds fabricated by electron beam melting for biomedical devices: mechanical and biological aspects, Sci. China Mater. 61 (2018) 455–474. https://doi.org/10.1007/s40843-017-9134-x.

[24] A. Safdar, L.Y. Wei, A. Snis, Z. Lai, Evaluation of microstructural development in electron beam melted Ti-6Al-4V, Mater. Charact. 65 (2012) 8–15. https://doi.org/10.1016/j.matchar.2011.12.008.

[25] N. Hrabe, T. Quinn, Effects of processing on microstructure and mechanical properties of a titanium alloy (Ti-6Al-4V) fabricated using electron beam melting (EBM), Part 2: Energy input, orientation, and location, Mater. Sci. Eng. A. 573 (2013) 271–277. https://doi.org/10.1016/j.msea.2013.02.065.

[26] L.E. Murr, S.M. Gaytan, D.A. Ramirez, E. Martinez, J. Hernandez, K.N. Amato, P.W. Shindo, F.R. Medina, R.B. Wicker, Metal Fabrication by Additive Manufacturing Using Laser and Electron Beam Melting Technologies, J. Mater. Sci. Technol. 28 (2012) 1–14. https://doi.org/10.1016/S1005-0302(12)60016-4.

[27] R. Laptev, N. Pushilina, E. Kashkarov, M. Syrtanov, E. Stepanova, A. Koptyug, A. Lider, Influence of beam current on microstructure of electron beam melted Ti-6Al-4V alloy, Prog. Nat. Sci. Mater. Int. 29 (2019) 440–446. https://doi.org/10.1016/j.pnsc.2019.04.011.

[28] Y. Bai, X. Gai, S. Li, L.C. Zhang, Y. Liu, Y. Hao, X. Zhang, R. Yang, Y. Gao, Improved corrosion behaviour of electron beam melted Ti-6Al–4V alloy in phosphate buffered saline, Corros. Sci. 123 (2017) 289–296. https://doi.org/10.1016/j.corsci.2017.05.003.

[29] B. Zhao, H. Wang, N. Qiao, C. Wang, M. Hu, Corrosion resistance characteristics of a Ti-6Al-4V alloy scaffold that is fabricated by electron beam melting and selective laser melting for implantation in vivo, Mater. Sci. Eng. C. 70 (2017) 832–841. https://doi.org/10.1016/j.msec.2016.07.045.

[30] J. Yang, H. Yang, H. Yu, Z. Wang, X. Zeng, Corrosion Behavior of Additive Manufactured Ti-6Al-4V Alloy in NaCl Solution, Metall. Mater. Trans. A Phys. Metall. Mater. Sci. 48 (2017) 3583–3593. https://doi.org/10.1007/s11661-017-4087-9.

[31] D.A. Puleo, A. Nanci, Understanding and controlling the bone-implant interface, Biomaterials. 20 (1999) 2311–2321. https://doi.org/10.1016/S0142-9612(99)00160-X.

[32] Y.Y. Heo, S. Um, S.K. Kim, J.M. Park, B.M. Seo, Responses of periodontal ligament stem cells on various titanium surfaces, Oral Dis. 17 (2011) 320–327. https://doi.org/10.1111/j.1601-0825.2010.01728.x.

[33] C. Mangano, A. De Rosa, V. Desiderio, R. d'Aquino, A. Piattelli, F. De Francesco, V. Tirino, F. Mangano, G. Papaccio, The osteoblastic differentiation of dental pulp stem cells and bone formation on different titanium surface textures, Biomaterials.

31 (2010) 3543–3551. https://doi.org/10.1016/j.biomaterials.2010.01.056.

[34] J.E. Davies, In vitro modeling of the bone/implant interface, Anat. Rec. 245 (1996) 426–445. https://doi.org/10.1002/(SICI)1097-0185(199606)245:2<426::AID-AR21>3.0.CO;2-Q.

[35] D.A. Puleo, L.A. Holleran, R.H. Doremus, R. Bizios, Osteoblast responses to orthopedic implant materials in vitro, J. Biomed. Mater. Res. 25 (1991) 711–723. https://doi.org/10.1002/jbm.820250603.

[36] C.H. Damsky, Extracellular matrix-integrin interactions in osteoblast function and tissue remodeling, Bone. 25 (1999) 95–96. https://doi.org/10.1016/S8756-3282(99)00106-4.

[37] D. Gutiérrez Zúñiga, J. Manrique Succar, C. Restrepo, J. Parvizi, J. Eduardo Manrique, Infecciones periprotésicas de cadera y rodilla: diagnóstico y manejo. Revisión de conceptos actuales, Rev. Colomb. Ortop. y Traumatol. 31 (2017) 87–92. https://doi.org/10.1016/j.rccot.2017.03.008.

[38] T. Lalani, V.H. Chu, C.A. Grussemeyer, S.D. Reed, M.P. Bolognesi, J.Y. Friedman, R.I. Griffiths, D.R. Crosslin, Z.A. Kanafani, K.S. Kaye, G. Ralph Corey, V.G. Fowler, Clinical outcomes and costs among patients with Staphylococcus aureus bacteremia and orthopedic device infections, Scand. J. Infect. Dis. 40 (2008) 973–977. https://doi.org/10.1080/00365540802245146.

[39] G.M. De Peppo, A. Palmquist, P. Borchardt, M. Lennerås, J. Hyllner, A. Snis, J. Lausmaa, P. Thomsen, C. Karlsson, Free-form-fabricated commercially pure Ti and Ti6Al4V porous scaffolds support the growth of human embryonic stem cell-derived mesodermal progenitors, ScientificWorldJournal. 2012 (2012). https://doi.org/10.1100/2012/646417.

[40] N.W. Hrabe, P. Heinl, R.K. Bordia, C. Körner, R.J. Fernandes, Maintenance of a bone collagen phenotype by osteoblast-like cells in 3D periodic porous titanium (Ti-6Al-4 V) structures fabricated by selective electron beam melting, Connect. Tissue Res. 54 (2013) 351–360. https://doi.org/10.3109/03008207.2013.822864.

[41] S. Ankem, C.A. Greene, Recent developments in microstructure/property relationships of beta titanium alloys, Mater. Sci. Eng. A. 263 (1999) 127–131. https://doi.org/10.1016/s0921-5093(98)01170-8.

[42] G. Del Guercio, M. Galati, A. Saboori, P. Fino, L. Iuliano, Microstructure and Mechanical Performance of Ti–6Al–4V Lattice Structures Manufactured via Electron Beam Melting (EBM): A Review, Acta Metall. Sin. (English Lett. 33 (2020) 183–203. https://doi.org/10.1007/s40195-020-00998-1.

[43] S.M.J. Razavi, B. Van Hooreweder, F. Berto, Effect of build thickness and geometry on quasi-static and fatigue behavior of Ti-6Al-4V produced by Electron Beam Melting, Addit. Manuf. 36 (2020) 101426. https://doi.org/10.1016/j.addma.2020.101426.

[44] V. Randle, O. Engler, Introduction to Texture Analysis, 2nd ed., USA, 2010.

[45] S. V. Scvortsova, M.A. German, I.A. Grushin, The structural and texture analysis of titanium alloy Ti-6Al-4V samples obtained by direct metal deposition, IOP Conf. Ser. Mater. Sci. Eng. 709 (2020). https://doi.org/10.1088/1757-899X/709/2/022081.

[46] M. Hoseini, P. Bocher, A. Shahryari, F. Azari, J.A. Szpunar, H. Vali, On the importance of crystallographic texture in the biocompatibility of titanium based substrate, J. Biomed. Mater. Res. - Part A. 102 (2014) 3631–3638. https://doi.org/10.1002/jbm.a.35028.

[47] M.R. Bache, W.J. Evans, Impact of texture on mechanical properties in an advanced titanium alloy, Mater. Sci. Eng. A. 319–321 (2001) 409–414. https://doi.org/10.1016/S0921-5093(00)02034-7.

[48] L.A.I. Kestens, H. Pirgazi, Texture formation in metal alloys with cubic crystal structures, Mater. Sci. Technol. (United Kingdom). 32 (2016) 1303–1315. https://doi.org/10.1080/02670836.2016.1231746.

[49] I. De-la-Pinta, M. Cobos, J. Ibarretxe, E. Montoya, E. Eraso, T. Guraya, G. Quindós, Effect of biomaterials hydrophobicity and roughness on biofilm development, J. Mater. Sci. Mater. Med. 30 (2019). https://doi.org/10.1007/s10856-019-6281-3.

[50] M. Sedlaček, P. Gregorčič, B. Podgornik, Use of the Roughness Parameters Ssk and Sku to Control Friction—A Method for Designing Surface Texturing, Tribol. Trans. 60 (2017) 260–266. https://doi.org/10.1080/10402004.2016.1159358.

[51] S.F. Lamolle, M. Monjo, S.P. Lyngstadaas, J.E. Ellingsen, H.J. Haugen, Titanium implant surface modification by cathodic reduction in hydrofluoric acid: Surface characterization and in vivo performance, J. Biomed. Mater. Res. - Part A. 88 (2009) 581–588. https://doi.org/10.1002/jbm.a.31898.

[52] E.J. Ekoi, A. Gowen, R. Dorrepaal, D.P. Dowling, Characterisation of titanium oxide layers using Raman spectroscopy and optical profilometry: Influence of oxide properties, Results Phys. 12 (2019) 1574–1585. https://doi.org/10.1016/j.rinp.2019.01.054.

[53] Y. Oshida, Materials Classification, in: Biosci. Bioeng. Titan. Mater., 2 nd, 2013: pp. 9–34. https://doi.org/10.1016/b978-0-444-62625-7.00002-9.

[54] K.K. Sankaran, R.S. Mishra, Titanium Alloys, 2017. https://doi.org/10.1016/b978-0-12-812068-2.00005-9.

[55] L.M. Kang, Y.J. Cai, X.C. Luo, Z.J. Li, X.B. Liu, Z. Wang, Y.Y. Li, C. Yang, Bimorphic microstructure in Ti-6Al-4V alloy manipulated by spark plasma sintering and in-situ press forging, Scr. Mater. 193 (2021) 43–48. https://doi.org/10.1016/j.scriptamat.2020.10.035.

[56] X. Luo, L.H. Liu, C. Yang, H.Z. Lu, H.W. Ma, Z. Wang, D.D. Li, L.C. Zhang, Y.Y. Li, Overcoming the strength–ductility trade-off by tailoring grain-boundary metastable Si-containing phase in β-type titanium alloy, J. Mater. Sci. Technol. 68 (2021) 112–123. https://doi.org/10.1016/j.jmst.2020.06.053.

[57] X. Wu, M. Yang, F. Yuan, G. Wu, Y. Wei, X. Huang, Y. Zhu, Heterogeneous lamella structure unites ultrafine-grain strength with coarse-grain ductility, Proc. Natl. Acad. Sci. U. S. A. 112 (2015) 14501–14505. https://doi.org/10.1073/pnas.1517193112.

[58] X. Wu, Y. Zhu, Gradient and lamellar heterostructures for superior mechanical

properties, MRS Bull. 46 (2021) 244–249. https://doi.org/10.1557/s43577-021-00056-w.

[59] M. Fousová, D. Vojtěch, J. Kubásek, E. Jablonská, J. Fojt, Promising characteristics of gradient porosity Ti-6Al-4V alloy prepared by SLM process, J. Mech. Behav. Biomed. Mater. 69 (2017) 368–376. https://doi.org/10.1016/j.jmbbm.2017.01.043.

[60] M. Radovic, E. Lara-Curzio, L. Riester, Comparison of different experimental techniques for determination of elastic properties of solids, Mater. Sci. Eng. A. 368 (2004) 56–70. https://doi.org/10.1016/j.msea.2003.09.080.

[61] A.K. Gain, L. Zhang, S. Lim, Tribological behavior of Ti–6Al–4V alloy: Subsurface structure, damage mechanism and mechanical properties, Wear. 464–465 (2021) 203551. https://doi.org/10.1016/j.wear.2020.203551.

[62] E.L. Odenberger, J. Hertzman, P. Thilderkvist, M. Merklein, A. Kuppert, T. Stöhr, J. Lechler, M. Oldenburg, Thermo-mechanical sheet metal forming of aero engine components in Ti-6Al-4V - PART 1: Material characterisation, Int. J. Mater. Form. 6 (2013) 391–402. https://doi.org/10.1007/s12289-012-1093-8.

[63] W.F. Ho, A comparison of tensile properties and corrosion behavior of cast Ti-7.5Mo with c.p. Ti, Ti-15Mo and Ti-6Al-4V alloys, J. Alloys Compd. 464 (2008) 580–583. https://doi.org/10.1016/j.jallcom.2007.10.054.

[64] L. Bolzoni, E.M. Ruiz-Navas, E. Gordo, Feasibility study of the production of biomedical Ti-6Al-4V alloy by powder metallurgy, Mater. Sci. Eng. C. 49 (2015) 400–407. https://doi.org/10.1016/j.msec.2015.01.043.

[65] I.H. Oh, N. Nomura, N. Masahashi, S. Hanada, Mechanical properties of porous titanium compacts prepared by powder sintering, Scr. Mater. 49 (2003) 1197–1202. https://doi.org/10.1016/j.scriptamat.2003.08.018.

[66] N.. study of the microstructure and hardness of two titanium alloys: C. pure and T.-6Al-4V Poondla, T.S. Srivatsan, A. Patnaik, M. Petraroli, A study of the microstructure and hardness of two titanium alloys: Commercially pure and Ti-6Al-4V, J. Alloys Compd. 486 (2009) 162–167.

https://doi.org/10.1016/j.jallcom.2009.06.172.

[67] P.K. Zysset, X.E. Guo, C.E. Ho, K.E. Moore, S.A. Goldstein, Elastic modulus and hardness of cortical and trabecular bone lamellae measured by nanoindentation in the human femur, 32 (1999) 1005–1012.

[68] T. Hanawa, Metal ion release from metal implants, Mater. Sci. Eng. C. 24 (2004) 745–752. https://doi.org/10.1016/j.msec.2004.08.018.

[69] T. Filippini, S. Tancredi, C. Malagoli, M. Malavolti, A. Bargellini, L. Vescovi, F. Nicolini, M. Vinceti, Dietary Estimated Intake of Trace Elements: Risk Assessment in an Italian Population, Expo. Heal. 12 (2020) 641–655. https://doi.org/10.1007/s12403-019-00324-w.

[70] J.F.E.C. on F. Additives, WHO Technical Report Series: Evaluation of certain food additives and contaminants: Seventy-Fourth Report of the Joint FAO/WHO Expert Committee on Food Additives, World Heal. Organ. - Tech. Rep. Ser. (2011) 1–133.

[71] S. Millour, L. Noël, A. Kadar, R. Chekri, C. Vastel, V. Sirot, J.C. Leblanc, T. Guérin, Pb, Hg, Cd, As, Sb and Al levels in foodstuffs from the 2nd French total diet study, Food Chem. 126 (2011) 1787–1799. https://doi.org/10.1016/j.foodchem.2010.12.086.

[72] I. Dimic, M. Rakin, B. Branko, Analysis of Metal Ion Release From Biomedical Implants, Met. Mater. Eng. 19(2) (2013) 167–176.

[73] T. Hanawa, Reconstruction and Regeneration of Surface Oxide Film on Metallic Materials in Biological Environments, Corros. Rev. 21 (2003) 161–182. https://doi.org/10.1515/CORRREV.2003.21.2-3.161.

[74] Y. Okazaki, E. Gotoh, Comparison of metal release from various metallic biomaterials in vitro, 26 (2005) 11–21. https://doi.org/10.1016/j.biomaterials.2004.02.005.

[75] S. Lanham-New, M. Alghamdi, J. Jalal, Nutritional aspects of bone, Encycl. Hum. Nutr. 3 (2013) 220–226. https://doi.org/10.1016/B978-0-12-375083-9.00029-5.

[76] T. Hanawa, Evaluation techniques of metallic biomaterials in vitro, Sci. Technol. Adv. Mater. 3. 3 (2002) 289–295. https://doi.org/https://doi.org/10.1016/S1468-6996(02)00028-1.

[77] M. Atapour, A.L. Pilchak, G.S. Frankel, J.C. Williams, Corrosion behavior of β titanium alloys for biomedical applications, Mater. Sci. Eng. C. 31 (2011) 885–891. https://doi.org/10.1016/j.msec.2011.02.005.

[78] J. Lu, P. Ge, Q. Li, W. Zhang, W. Huo, J. Hu, Y. Zhang, Y. Zhao, Effect of microstructure characteristic on mechanical properties and corrosion behavior of new high strength Ti-1300 beta titanium alloy, J. Alloys Compd. 727 (2017) 1126–1135. https://doi.org/10.1016/j.jallcom.2017.08.239.

[79] S. Bahl, S. Suwas, K. Chatterjee, The importance of crystallographic texture in the use of titanium as an orthopedic biomaterial, RSC Adv. 4 (2014) 38078–38087. https://doi.org/10.1039/c4ra05440g.

[80] I.D. Dimć, I.L. Cvijović-Alagić, M.B. Rakin, A.A. Perić-Grujić, M.P. Rakin, B.M. Bugarski, S.S. Putić, Effect of the pH of artificial saliva on ion release from commercially pure titanium, Acta Period. Technol. 44 (2013) 207–215. https://doi.org/10.2298/APT1344207D.

[81] L.L. Wong, S.I. Martin, R.B. Rebak, Methods to calculate corrosion rates for alloy 22 from polarization resistance experiments, Am. Soc. Mech. Eng. Press. Vessel. Pip. Div. PVP. 2006 (2006). https://doi.org/10.1115/PVP2006-ICPVT-11-93421.

[82] G. of roughness on electrochemical and pitting corrosion of T.-6Al-4V alloy in 12 wt. . Hc. solution at 35»°C Chi, D. Yi, H. Liu, Effect of roughness on electrochemical and pitting corrosion of Ti-6Al-4V alloy in 12 wt.% HCl solution at 35°C, J. Mater. Res. Technol. 9 (2020) 1162–1174. https://doi.org/10.1016/j.jmrt.2019.11.044.

[83] J.C. Wang, Y.J. Liu, P. Qin, S.X. Liang, T.B. Sercombe, L.C. Zhang, Selective laser melting of Ti–35Nb composite from elemental powder mixture: Microstructure, mechanical behavior and corrosion behavior, Mater. Sci. Eng. A. 760 (2019) 214–224. https://doi.org/10.1016/j.msea.2019.06.001.

[84] E.T. Uzumaki, C.S. Lambert, A.R.S. Jr, C.A.C. Zavaglia, Surface properties and cell behaviour of diamond-like carbon coatings produced by plasma immersion, 515 (2006) 293–300. https://doi.org/10.1016/j.tsf.2005.12.081.

[85] C. Wirth, V. Comte, C. Lagneau, P. Exbrayat, M. Lissac, Nitinol surface roughness modulates in vitro cell response : a comparison between fibroblasts and osteoblasts, 25 (2005) 51–60. https://doi.org/10.1016/j.msec.2004.06.001.

[86] W. Teughels, N. Van Assche, I. Sliepen, M. Quirynen, Effect of material characteristics and / or surface topography on biofilm development, Clin. Oral Implants Res. 17 (2006) 68–81. https://doi.org/https://doi.org/10.1111/j.1600-0501.2006.01353.x.

[87] V.K. Truong, R. Lapovok, Y.S. Estrin, S. Rundell, J.Y. Wang, C.J. Fluke, R.J. Crawford, E.P. Ivanova, The influence of nano-scale surface roughness on bacterial adhesion to ultrafine-grained titanium, Biomaterials. 31 (2010) 3674–3683. https://doi.org/10.1016/j.biomaterials.2010.01.071.

[88] C. Nelson, Y. Oshida, J. Henrique, C. Lima, C. Alberto, Relationship between surface properties (roughness , wettability and morphology) of titanium and dental implant removal torque, J. Mech. Behav. Biomed. Mater. I. 1 (2008) 234–242. https://doi.org/10.1016/j.jmbbm.2007.12.002.

[89] N. Cerca, G.B. Pier, M. Vilanova, R. Oliveira, J. Azeredo, Quantitative analysis of adhesion and biofilm formation on hydrophilic and hydrophobic surfaces of clinical isolates of Staphylococcus epidermidis, 156 (2005) 506–514. https://doi.org/10.1016/j.resmic.2005.01.007.

[90] E.P. Ivanova, V.K. Truong, J.Y. Wang, C.C. Berndt, R.T. Jones, I.I. Yusuf, I. Peake, H.W. Schmidt, C. Fluke, D. Barnes, R.J. Crawford, Impact of Nanoscale Roughness of Titanium Thin Film Surfaces on Bacterial Retention, 26 (2010) 1973–1982. https://doi.org/10.1021/la902623c.

[91] P. Szymczyk-Ziółkowska, V. Hoppe, M. Rusińska, J. Gasiorek, G. Ziółkowski, K. Dydak, J. Czajkowska, A. Junka, The impact of ebm-manufactured ti6al4v eli alloy surface modifications on cytotoxicity toward eukaryotic cells and microbial biofilm

formation, Materials (Basel). 13 (2020) 1–21. https://doi.org/10.3390/ma13122822.

[92] Y. Wu, J.P. Zitelli, K.S. Tenhuisen, X. Yu, M.R. Libera, Differential response of Staphylococci and osteoblasts to varying titanium surface roughness, Biomaterials. 32 (2011) 951–960. https://doi.org/10.1016/j.biomaterials.2010.10.001.

[93] J. Oh, H. Cha, J.H. Reed, A.E. Gonsalves, J.K. Roma, C.E. Dana, M. Toc, S. Hong, J.B. Ho, J.E. Andrade, K.D. Jo, M. Alleyne, N. Miljkovic, D.M. Cropek, Ultrascalable Multifunctional Nanoengineered Copper and Aluminum for Antiadhesion and Bactericidal Applications, ACS Appl. Bio Mater. 2 (2019) 2726–2737. https://doi.org/10.1021/acsabm.8b00765.

[94] A. Di Cerbo, A. Mescola, R. Iseppi, R. Canton, G. Rossi, R. Stocchi, A.R. Loschi, A. Alessandrini, S. Rea, C. Sabia, Antibacterial Effect of Aluminum Surfaces Untreated and Treated with a Special Anodizing Based on Titanium Oxide Approved for Food Contact, Biology (Basel). 9 (2020) 456–473. https://doi.org/doi:10.3390/biology9120456.